



# Physics of notochord tube expansion in ascidians

Wenjie Shi<sup>a,b,1</sup> , Charlie Duclut<sup>c,1,2</sup> , Yan Xu<sup>a,1</sup> , Yuanting Ma<sup>a</sup> , Jinghan Qiao<sup>a</sup>, Boyan Lin<sup>a</sup>, Dongyu Yang<sup>a</sup>, Jacques Prost<sup>c,d</sup> , and Bo Dong<sup>a,b,e,2</sup>

Affiliations are included on p. 12.

Edited by Raymond E. Goldstein, University of Cambridge, Cambridge, United Kingdom; received September 30, 2024; accepted April 9, 2025 by Editorial Board Member Daan Frenkel

**Interaction of cells and the surrounding lumen drives the formation of tubular system that plays the transport and exchange functions within an organism. The physical and biological mechanisms of lumen expansion have been explored. However, how cells communicate and coordinate with the surrounding lumen, leading to continuous tube expansion to a defined geometry, is crucial but remains elusive. In this study, we utilized the ascidian notochord tube as a model to address the underlying mechanisms. We first quantitatively measured and calculated the geometric parameters and found that tube expansion experienced three distinct phases. During the growth processes, we identified and experimentally demonstrated that both Rho GTPase Cdc42 signaling-mediated cell cortex distribution and the stability of tight junctions (TJs) were essential for lumen opening and tube expansion. Based on these experimental data, a conservation-laws-based tube expansion theory was developed, considering critical cell communication pathways, including secretory activity through vesicles, asymmetric cortex tension driven anisotropic lumen geometry, as well as the TJs gate barrier function. Moreover, by estimating the critical tube expansion parameters from experimental observation, we successfully predicted tube growth kinetics under different conditions through the combination of computational and experimental approaches, highlighting the coupling between actomyosin-based active mechanics and hydraulic processes. Taken together, our findings identify the critical cellular regulatory factors that drive the biological tube expansion and maintain its stability.**

physical model | tube expansion | Cdc42 | notochord | tight junctions

Tubular networks, prevalent in various organ systems (1–4), play vital roles in physiological functions, including the conservation and transport of gases, liquids, biomacromolecules, and cells (1). The formation and expansion of these tubes involve numerous cellular processes, such as polarized protein transport (4), tight junctions (TJs) formation (5, 6), symmetry breaking (3, 7), and cytoskeletal dynamics (8). These tubular structures can act as biochemical signal centers to guide tissue patterning (9), alter cell fate and behavior through mechanotransduction (10, 11), or even function as a hydrostatic skeleton for larval swimming (12). Conversely, loss of control over tube size and geometry can lead to defects or even diseases like polycystic kidney disease and lymphatic stenosis (1).

Cell interactions with the surrounding lumen drive the formation of tubular systems. A key question is how cells regulate lumen growth to an appropriate size for optimal function. Given that lumen expansion is a hydraulic process, active solute accumulation plays a significant role in establishing an osmotic pressure gradient. The difference in ionic concentration between intercellular and intracellular spaces, generated by ionic pumps, can drive passive water flux (13). Water accumulation has been studied in the formation of the zebrafish otic vesicle (14, 15), Kuppfer's vesicle (16), and even in mammalian embryo size control (17). Many studies have measured the typical pumping rate of ion transporters (18–20), and inhibiting activity blocks lumen formation (21). To understand how ionic flow creates positive osmotic pressure and promotes water accumulation, quantitative simulations and biophysical models have been developed (22). Another mechanism involves transporting osmolytes through the secretory system. The release of cytoplasmic vesicle has been observed in the initiation of various lumen systems (10, 23), but their biological and physical functions in lumen inflation and maturation remain unclear. Despite the passive water flux driven by the solute density-mediated osmotic gradient, fluid and ion leakage through cell–cell clefts are also vital in determining the stable lumen size (22). Paracellular leakage depends on the permeability of TJs. Different TJs protein compositions can be selectively permeable to different cations/anions or even water (5, 6, 24). However, few studies have explored how cells regulate the gate barrier function of TJs to control lumen size.

## Significance

Geometry and morphology are crucial for tubular network to perform physiological functions in circulatory and respiratory systems. However, the underlying control mechanisms remain largely unknown. In this study, we found that Rho signaling-regulated cortex contractility tension and cell tight junctions were two significant ways in controlling tube geometry and size using a notochord tubulogenesis model in marine ascidian. We further developed a general theoretical model based on the conservation-law and the experimental data. The numerical model could successfully predict lumen growth phenotypes when cellular processes are out of regulation. Our study gives explicit molecular and mechanical mechanisms on how cell–lumen interaction can regulate tube expansion and establishes a more general tube expansion model, which can provide cues for pathogenesis identification.

Author contributions: J.P. and B.D. designed research; W.S., C.D., Y.X., Y.M., J.Q., B.L., D.Y., and J.P. performed research; W.S., C.D., Y.X., Y.M., J.Q., B.L., D.Y., J.P., and B.D. analyzed data; and W.S., C.D., J.P., and B.D. wrote the paper.

The authors declare no competing interest.

This article is a PNAS Direct Submission. R.E.G. is a guest editor invited by the Editorial Board.

Copyright © 2025 the Author(s). Published by PNAS. This open access article is distributed under [Creative Commons Attribution-NonCommercial-NoDerivatives License 4.0 \(CC BY-NC-ND\)](https://creativecommons.org/licenses/by-nc-nd/4.0/).

<sup>1</sup>W.S., C.D., and Y.X. contributed equally to this work.

<sup>2</sup>To whom correspondence may be addressed. Email: charlie.duclut@curie.fr or boding@ouc.edu.cn.

This article contains supporting information online at <https://www.pnas.org/lookup/suppl/doi:10.1073/pnas.2419960122/-DCSupplemental>.

Published June 5, 2025.

Understanding how cells control lumen geometry is a significant question. Biological tubes, such as blood vessel networks and *Drosophila* trachea, often exhibit anisotropic geometry or heterogeneity during growth (25, 26), but the underlying mechanical mechanisms remain largely unknown. In multicellular lumens, studies have shown that cell mitosis, epithelial thinning, and pressure-driven vascular network remodeling by blood flow can regulate anisotropic tube geometry (27, 28). Another study on hepatocyte doublets revealed that integrin-based adhesion induces anisotropic mechanical stress and drives lumen elongation in a specific direction (7). Cells generate mechanical forces to the lumen boundary through different mechanisms. Forces at the junctions between several cells, summarized in the Young–Dupré equation, are especially important and can deform the lumen into a specified shape. However, it remains largely unknown how cells precisely control these forces to shape a tubular organ.

In this study, we utilized an emerging tubulogenesis model in the ascidian notochord (12, 29, 30), in which lumen pockets first appeared between pairs of notochord cells and then coalesced into a multicellular tube (Fig. 1A), providing an ideal simple model system for tube formation. We showed that actomyosin contractility activity was a crucial mechanism for regulating lumen geometry. We measured and theoretically calculated the cortex contractility tension at the tube boundary, establishing a correlation between tension value and tube geometry. We identified the regulatory role of Rho signaling Cdc42, which determines the cortex actomyosin distribution, and experimentally confirmed the importance of the TJs gate barrier function in controlling lumen size. Using these experimental results, we constructed a general tube expansion model that considers cell–lumen interactions, including pumping activity, cortex tension at the tube boundary, and TJs gate barrier function. We quantitatively simulated the tube expansion processes and further predicted the tube expansion dynamics based on experimental

data in wild type conditions and on the calculated value of model parameters. In addition, we used our theoretical and numerical model to reproduce the tube expansion dynamics in perturbed conditions. Our model results and their comparison to experimental data underline the interplay between active mechanics driven by the acto-myosin cortex and active hydraulic transport at the lumen surface. Finally, our approach allows us to identify the key processes during tube expansion and to delimitate the theoretical parameter range to maintain tube stability.

## Results

**Sequential Expansion of Pocket Lumen in *Ciona* Notochord.** During *Ciona* embryogenesis, a model organism in ascidian, notochord cells undergo sequential steps to elongate along the anterior–posterior (A–P) axis (Fig. 1 A and B and *SI Appendix*, Fig. S1 A and B). This includes convergent extension, circumferential constriction by the equatorial contractile ring, and a mesenchymal–endothelial transition driven by de novo tubulogenesis (32) (Fig. 1A). Assisted by Par complex localization and the formation of a TJ ring (33), lumen pockets emerge at the center of the lateral domain at both A–P ends of a notochord cell (Fig. 1 B–B'' and *SI Appendix*, Fig. S1C). These pocket lumens expand to a relatively constant volume within 2 h (Fig. 1 A, Top; Fig. 1 B–B'' and *SI Appendix*, Fig. S1 D–G). Simultaneously, the TJs ring expands to accommodate the continuously growing volume (33). As the notochord cell shape changes, the vertical axes of the lumen begin to tilt in alternating directions (Fig. 1 A, Bottom Left and *SI Appendix*, Fig. S1H). Eventually, all pocket lumens coalesce (Fig. 1 A, Bottom Middle) into a continuous single lumen along the A–P axis (Fig. 1 A, Bottom Right and *SI Appendix*, Fig. S1I).

To comprehend the precise expansion of the lumen during tubulogenesis, we observed and quantified various lumen shapes

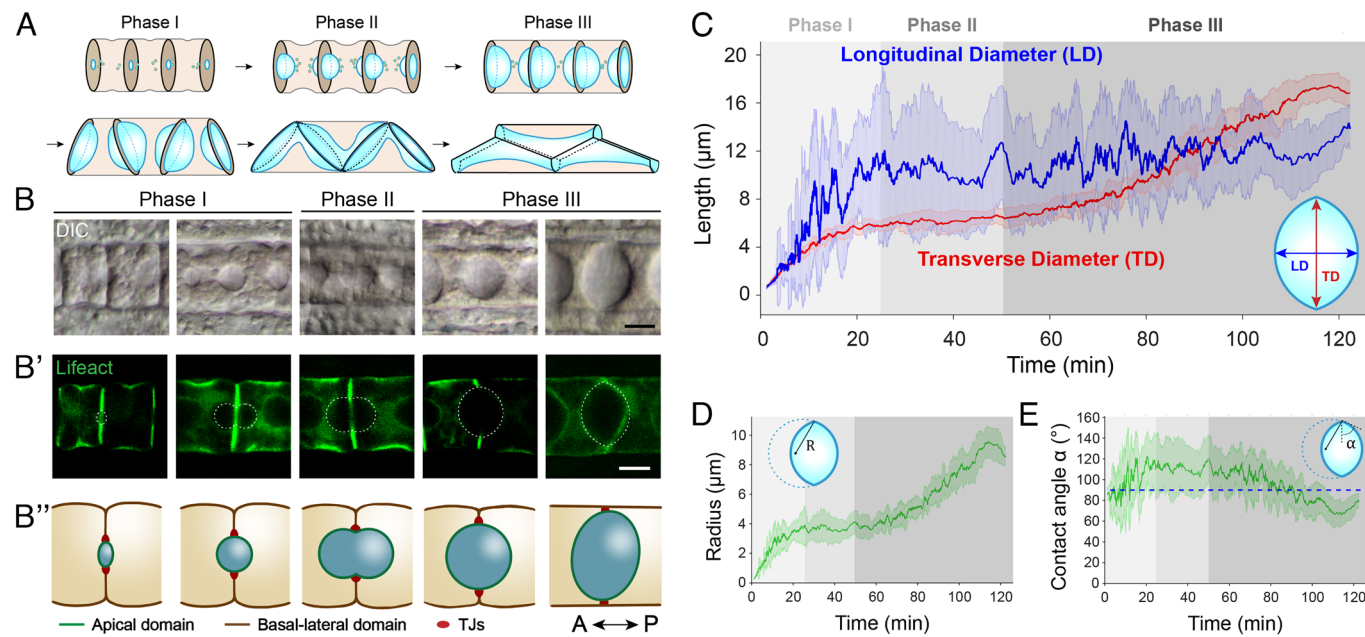


**Fig. 1.** Quantitative analysis of lumen expansion with combined symmetrical spherical cap shape. (A) The schematic diagram illustrates notochord tubulogenesis in *Ciona* embryonic and larval development. (B) A differential interference microscopy (DIC) image, a 2D confocal section (B'), and a schematic representation (B'') show exemplary lumen shapes and sizes at different time periods. Dashed lines in (B') indicate the lumen boundary. (C) Quantitative statistics of lumen TD and LD (mean  $\pm$  SD) are presented as a function of time ( $n = 1,180$  lm,  $N = 20$  embryo batches). The Inset in (C) shows the definition of the geometric parameters. The gray shaded areas indicate the three different phases discussed in the text. Measurements were done on stilled embryos, and each sample was backdeduced to the growing time point based on the relationship between TD and time (31). (D) Quantitative statistics of the radius of curvature  $R$  of the lumen (mean  $\pm$  SD) for the samples described in (C) ( $n = 1,180$  lm,  $N = 20$  embryo batches). The Inset in (D) shows the definition of the radius of curvature  $R$ . (E) Quantitative statistics of the lumen contact angle  $\alpha$  (mean  $\pm$  SD) for the samples described in (C) ( $n = 1,180$  lm,  $N = 20$  embryo batches). The Inset in (E) shows the definition of the lumen contact angle  $\alpha$ . [Scale bars, 10 μm in (B) and (B'').]

(*SI Appendix*, Fig. S2). We simplified the lumen as two combined symmetrical spherical caps (Fig. 1 C, *Inset*) and measured the characteristic parameters: radius of curvature  $R$  and contact angle  $\alpha$  (Fig. 1 D and E). Using simple geometry, we calculated the transverse diameter (TD) (red in Fig. 1C) and longitudinal diameter (LD, diameter on the axial axis, blue in Fig. 1C). We observed that the lumen volume and surface area grew steadily, except for a plateau period at around 25 to 60 min (*SI Appendix*, Fig. S3 E and G). We also measured the notochord cell length (*SI Appendix*, Fig. S3 A and B), surface area (*SI Appendix*, Fig. S3 C, D, and F), and volume (*SI Appendix*, Fig. S3 H–I) for reference. We found that TD and LD exhibited different growth patterns (Fig. 1C), leading to sequential lumen expansion dynamics. We defined three growth phases: during the initiation phase of tube expansion (0 to 25 min, phase I), the lumen grows rapidly in volume. Its geometry, initially stretched along the cell–cell contact direction and showing a convex-lens shape ( $\alpha$  is around 85°), then becomes more elongated in the longitudinal direction. At the end of this first phase, the lumen has a peanut shape due to the large contact angle ( $\alpha$  is larger than 90°). In the middle phase (25 to 60 min, phase II), the lumen reaches a relative steady-state during which the radius and contact angle remain constant. The lumen remains pinched at the cell–cell contact. In the maturation phase (60 to 130 min, phase III), the lumen grows steadily and transitions back into an elongated shape along the cell–cell contact direction (convex-lens shape,  $\alpha$  becomes smaller than 90°). To understand the key biological mechanisms regulating lumen geometry and size, we investigated the underlying regulatory factors involved in the expansion process.

**Cortex Fluorescence Signal Is Dynamical and Correlates with Tube Expansion Phases.** In the *Ciona* notochord, a pocket lumen is encircled by two adjacent cells. Our previous study found that changes in myosin contractility significantly influenced lumen growth kinetics (31), leading us to hypothesize that the actomyosin–activated contractility tension might be a key determinant of lumen geometry. It is now well-established that the acto-myosin cortex is responsible for the coarse-grained surface tension (34, 35), thus the dynamical localization of F-actin and myosin signals is good proxy for estimating cortical tension. We labeled the notochord cell cortex using electroporation of Lifeact-eGFP and tdTomato-MRLC (myosin regulatory light chain), driven by the notochord–specific promoter *Brachyury*. Lifeact and MRLC labeled the polymerized actin and myosin motors, respectively. We observed that the cell cortex aggregated at the lateral-apical domain boundary, forming a ring-like structure (*SI Appendix*, Fig. S4 A and A'), suggesting that the actomyosin contractile ring may regulate lumen geometry. To test this hypothesis, we quantitatively measured the actin fluorescence intensity at the baso–lateral domain (*SI Appendix*, Fig. S4 A and A'), using an asymmetric tri-Gaussian distribution (36) (*SI Appendix*, Figs. S2 A and B and S4 B–F). We furthermore quantified actin and myosin colocalization using the same technique (*SI Appendix*, Fig. S6). We then calculated the relative actomyosin fluorescence intensity, which serves as a measure of active contractility tension, at the lateral–lumen boundary.

Using the tri-Gaussian distribution fitting, we extracted six characteristic parameters of F-actin and myosin distribution (Fig. 2 C–H and *SI Appendix*, Figs. S5 and S6 B–G, and Movie S1): the equatorial contractile ring overactivity and SD, the anterior–lateral contractile ring overactivity and SD, and the posterior–lateral contractile ring overactivity and SD (definitions in Fig. 2B and *SI Appendix*, Fig. S4F). The average tri-Gaussian distribution in each phase is shown in Fig. 2I. We further calculated

the relative tube boundary cortex fluorescence intensity as a measure of active contractility tension. The result indicates a high correlation between the lumen contact angle and either actin activity (Fig. 2J) or myosin activity (Fig. 2K). In the early phase, the tube boundary actomyosin fluorescence intensity (blue line in Fig. 2J and K) starts from a low level, coinciding with the stretched lumen geometry along the cell–cell contact direction during tubulogenesis ( $\alpha < 90^\circ$ , red line in Fig. 2 J and K). In phase II and III, the boundary fluorescence intensity first increases and reaches a peak, then drops, which also corresponds to the transition of lens shape (phase II) to peanut shape (phase III). Moreover, we found that the tube boundary cortex fluorescence intensity correlates with the lumen opening velocity (TD growing velocity). The statistical results (Fig. 2L) showed that TD has a very low average growing velocity ( $0.08 \pm 0.02 \mu\text{m}/\text{min}$ ) under high boundary tension (over 4.1 a.u.), but, the growing velocity is three times higher ( $0.24 \pm 0.10 \mu\text{m}/\text{min}$ ) under low boundary tension (below 4.1 a.u.).

In summary, our quantitative measurements of the cortex actomyosin fluorescence intensity at the tube boundary seem to indicate the presence of a bilateral actomyosin ring that dynamically assembles and disassembles during the different phases of lumen formation and growth. The line tension that actomyosin rings generate is highly correlated with lumen contact angle and TD growing velocity, highlighting its crucial role in regulating tube growing kinetics and ultimately determining the tube geometry.

**Rho Signaling Is Responsible for Enrichment of Actomyosin at Contractile Ring and Regulates Cortex Tension.** Rho GTPases are considered to be the most significant signaling mechanisms that regulate cell cytoskeleton and tube morphogenetic responses (37). Precise measurements and numerical models have shown that Rho GTPases localize at actomyosin-enriched positions (36, 38, 39). To understand how the actomyosin cortex is assembled to accurately regulate lumen geometry, we examined the Rho GTPases that are highly expressed in the *Ciona* notochord (40), and further screened to identify which one plays a crucial role in regulating actomyosin dynamics.

Cdc42 is one of the most important proteins in the family of Rho GTPases, which is known to regulate basic biological processes by promoting cytoskeleton-based changes in the cell cortex (41–43), including in initiating microlumen formation (44). Our preliminary labeling by GFP fusion protein showed that Cdc42 signal is mainly in cytoplasm and on cell cortex, especially on apical domain (Fig. 3 A, *Top-Left*), showing a potential role in regulating lumen formation. To further understand the function of Cdc42 in *Ciona* notochord, we designed two experiments to perturb the normal gene function: either using a constitutively active form (CA, a mutated version of the protein that is always in an active state) or using a dominant negative form (DN, a mutated version that lacks normal function but still interacts with other proteins or complexes, blocking their activity).

Upon examining the phenotype of Cdc42 CA/DN–transfected cells in the *Ciona* notochord, we found that both CA and DN forms of Cdc42 led to a complete disruption of notochord cell behaviors: in most cases (276/334 Cdc42 DN-expressing notochord cells for statistics), notochord cell even failed to form a single-layer structure, and lumen at cell–cell junctions were misplaced or nonexistent (Fig. 3 A, *Top-Right* and *Bottom*). In rare cases (32/334 Cdc42 DN-expressing notochord cells), the morphological structure resembled that of the wild type (WT) (Fig. 3 A, *Bottom Right*), although the actomyosin distribution was altered and showed a negative correlation with Cdc42 DN distribution (arrows in Fig. 3 A and C), while cortex distribution in Cdc42 WT-transfected cells remained unchanged (Fig. 3B). We

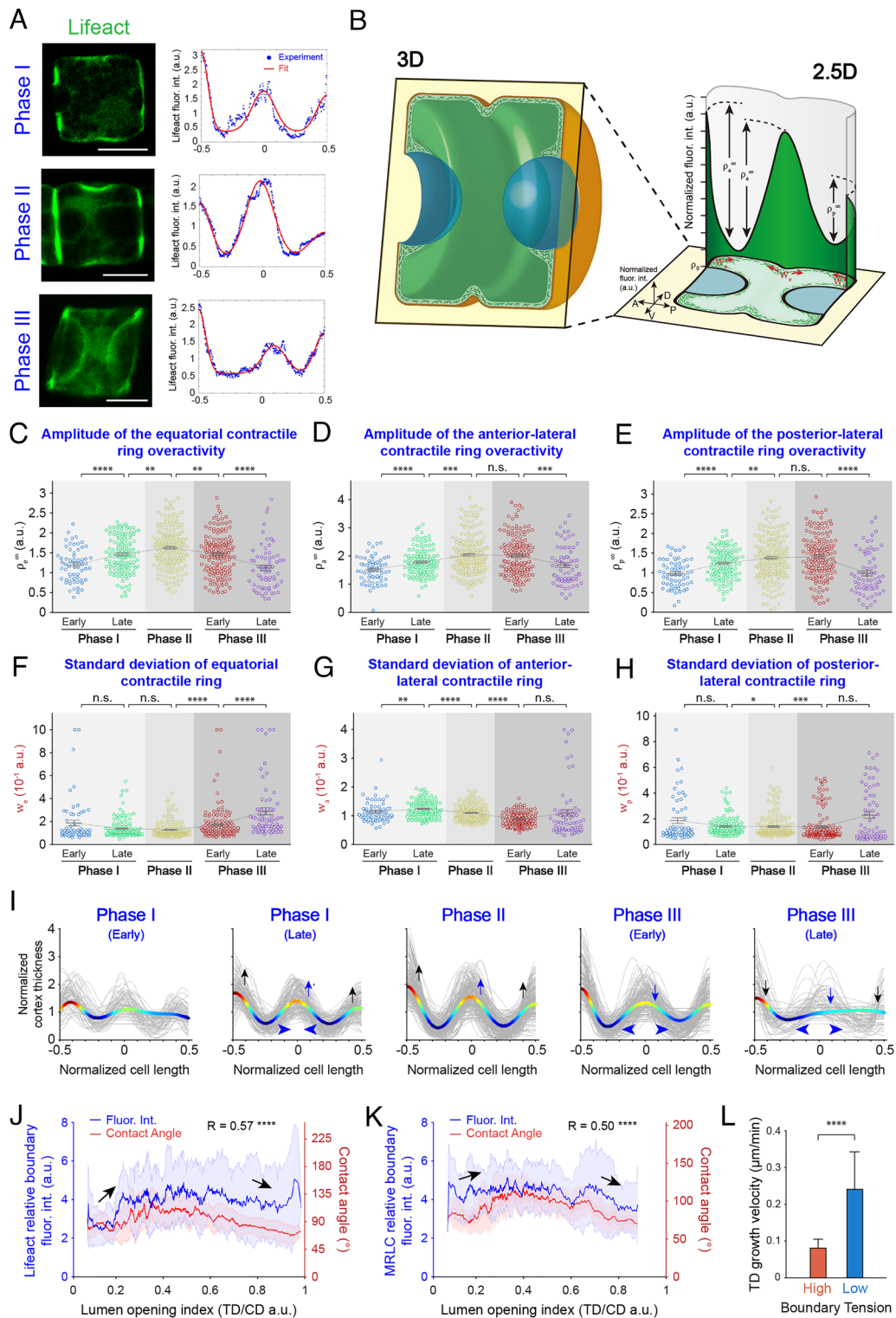


**Fig. 2.** Correlation of tube boundary actomyosin cortex fluorescence intensity with lumen geometry and growth. (A) Confocal images (section, Left) and basal-lateral domain Tri-Gaussian distribution fitting (Right) display exemplary lumen geometry and cortex distribution in the early, middle, and late phases of lumen expansion, respectively. Lifeact-EGFP indicates F-actin localization. Blue dots represent the raw measurement of fluorescence intensity, while red lines represent the fitting curves. (B) 3D (Left) and 2.5D (Right) schematic representations illustrate the method for measuring and fitting notochord cell basal-lateral domain cortex fluorescence intensity. Blue, green, and orange colors indicate the localization of the lumen, cortex, and cell membrane, respectively. The yellow plane shows the maximum sagittal section. The X, Y, and Z axes in the 2.5D schematic representation indicate the A-P axis, DV axis, and the normalized fluorescence intensity, respectively.  $\rho_a^\infty$ ,  $\rho_e^\infty$ , and  $\rho_p^\infty$  represent the overactivity of the Tri-Gaussian distribution, while  $w_a^\infty$ ,  $w_e^\infty$ , and  $w_p^\infty$  represent the SD. (C–H) Data statistics of characteristic parameters (mean  $\pm$  SEM) of the equatorial contractile ring and bilateral contractile ring (amplitude of overactivity and SD) in five different stages (n in each stage are 102, 220, 183, 104, 46 cells, respectively, N = 20 embryo batches). (I) Average cortex thickness distribution in each growing stage. The colored lines show the average cortex thickness distribution, while the gray lines show cortex thickness distribution from individuals. (J and K) Normalized tube boundary cortex fluorescence intensity (blue line) by Lifeact (J) or MRLC (K) and lumen contact angle (red line) as a function of the lumen opening index (mean  $\pm$  SD). (L) Influence of lumen boundary tension on lumen growth velocity in the radial axis. The Mann-Whitney U-test and Student t test are used, depending on whether data shows normality distribution (C–H and L),  $\rho$  Spearman correlation test (J and K). \* $P < 0.05$ , \*\* $P < 0.01$ , \*\*\*\* $P < 0.0001$ . [Scale bars, 10  $\mu\text{m}$  in (A).]

quantitatively measured the actomyosin distribution phenotype and found that the amplitude of overactivity of the bilateral contractile ring was significantly reduced, and that of the equatorial contractile ring only had a slight reduction (Fig. 3D), while the SD of all three contractile rings significantly increased (Fig. 3E).

In addition, a systematic screening of multiple other Rho GTPases showed that neither the overexpression of (WT form nor the DN form) had noticeable phenotypes (SI Appendix, Fig. S7). These results suggest that Cdc42 is the primary Rho upstream signaling that assembles the actomyosin-enriched contractile ring and regulates the sequential change of cortex thickness at the tube boundary.

**TJs Serve as Physical Barriers that Regulates Fluid Leakage.** Considering that the tube in the *Ciona* notochord is an intercellular tube, water and ion leakage through cell–cell cleavage may impact tube volume and lumen expansion kinetics (5, 22). The gate barrier function of TJs is a well-documented fact (5), and perturbations of different components of TJ complex are known to lead to leakage or higher permeability (45, 46). We therefore monitored TJs using a ZO1 fluorescent fusion protein (33, 47), which specifically localizes at the junction of the lateral domain and the apical domain (Fig. 4 B and B', Left). Interestingly, we found that the disruption of TJs obtained by

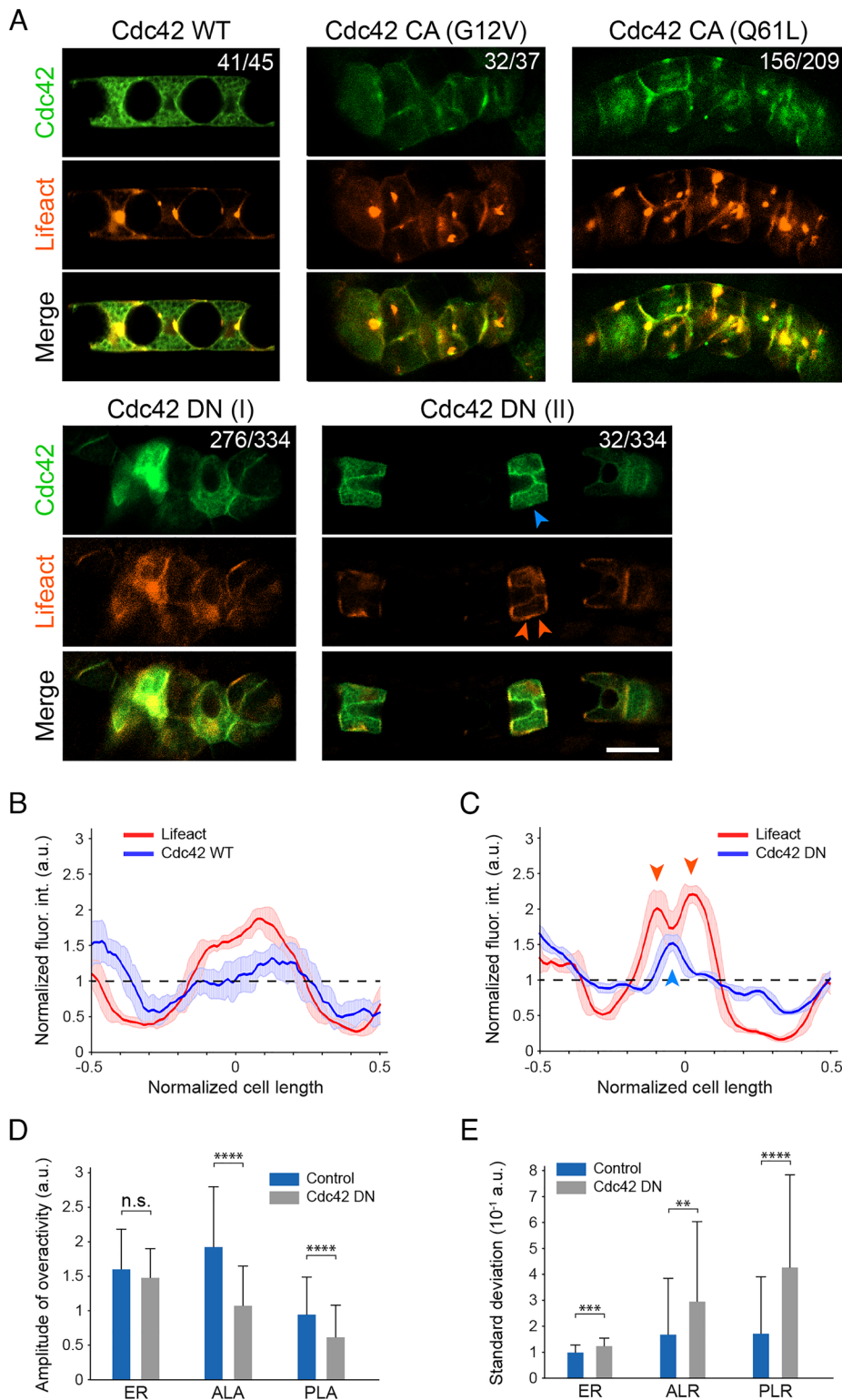


**Fig. 3.** Cdc42 as the primary upstream Rho signal controlling cortex thickness distribution in *Ciona* notochord. (A) Confocal images of notochord cells expressing GFP-Cdc42 WT, GFP-Cdc42 CA (G12V and Q61L), and GFP-Cdc42 DN (D118A). The notochord cell cortex was marked by lifeact-tdTomato. The blue and red arrowheads indicate noncolocalization between GFP-Cdc42 DN and lifeact-tdTomato. Cdc42 CA transfected cells are unable to form a lumen, as well as most of the DN transfected cells [Cdc42 DN (I)]. One tenth of the DN transfected cells did form a lumen with abnormal geometry [Cdc42 DN (II)]. ( $n = 45, 37, 209, 334$  cells,  $N = 3, 3, 6, 5$  embryo batches for Cdc42 WT, Cdc42 G12V, Cdc42 Q61L, and Cdc42 DN, respectively). (B) Normalized lifeact-tdTomato and GFP-Cdc42 WT fluorescence intensity (mean  $\pm$  SD) throughout the basal-lateral domain. (C) Normalized lifeact-tdTomato and GFP-Cdc42 DN (II) fluorescence intensity (mean  $\pm$  SD) throughout the basal-lateral domain. The blue and red arrows represent the negative correlation between Cdc42 DN and F-actin, consistent with the arrowheads in (A). (D) Quantification of the amplitude of overactivity of the equatorial contractile ring and bilateral contractile ring (mean  $\pm$  SD) in the control group and Cdc42 DN (II)-transfected group. ER represents equatorial contractile ring; ALR, represents the anterior-lateral contractile ring; PLR represents posterior-lateral contractile ring ( $n = 558, 58$  cells for the control group and Cdc42 DN-transfected group, respectively,  $N = 20$ , five embryo batches for the control group and Cdc42 DN-transfected group, respectively). (E) Quantification of the SD of the equatorial contractile ring and bilateral contractile ring (mean  $\pm$  SD) in the control group and Cdc42 DN (II)-transfected group for the samples described in (D). The Mann-Whitney U-test and Student *t* test are used, depending on whether data shows normality distribution (D and E). \**P* < 0.05, \*\*\**P* < 0.001, \*\*\*\**P* < 0.0001. [Scale bar, 20  $\mu$ m in (A).]

overexpression of the DN forms of ZO1, either ZO1<sup>ΔABR</sup> or ZO1<sup>ΔU5-GuK</sup> (Fig. 4*A*), led to smaller lumen pockets or even no lumen phenotypes. In both cases, the lumen membrane was however present, but the lumen pocket failed to expand (Fig. 4*B* and *B'*, *Middle* and *Right*), suggesting that the lumen is not sufficiently tight to accumulate fluid.

To quantitatively analyze the influence of TJs on lumen formation, we precisely measured the lumen volume, TD and LD. Importantly, overexpression of ZO1 DN forms significantly reduced the lumen volume by more than 50% compared to the

ZO1 WT group (Fig. 4*E*). Interestingly, this loss of volume can be mainly explained by a decrease of the LD by 2 to 3 times (Fig. 4*D*), while the TD was relatively unaffected by the overexpression of ZO1 (Fig. 4*C*). Furthermore, we also looked at the overexpression of the ZO1 WT and found that lumen volume was not significantly modified, but a slight change in the lumen geometry with a slightly larger LD and smaller TD compared to control (*SI Appendix*, Fig. S8). These results suggest that the stability of the TJs is essential to control the lumen volume, most likely by preventing water and solute leakage from the cell–cell cleft.

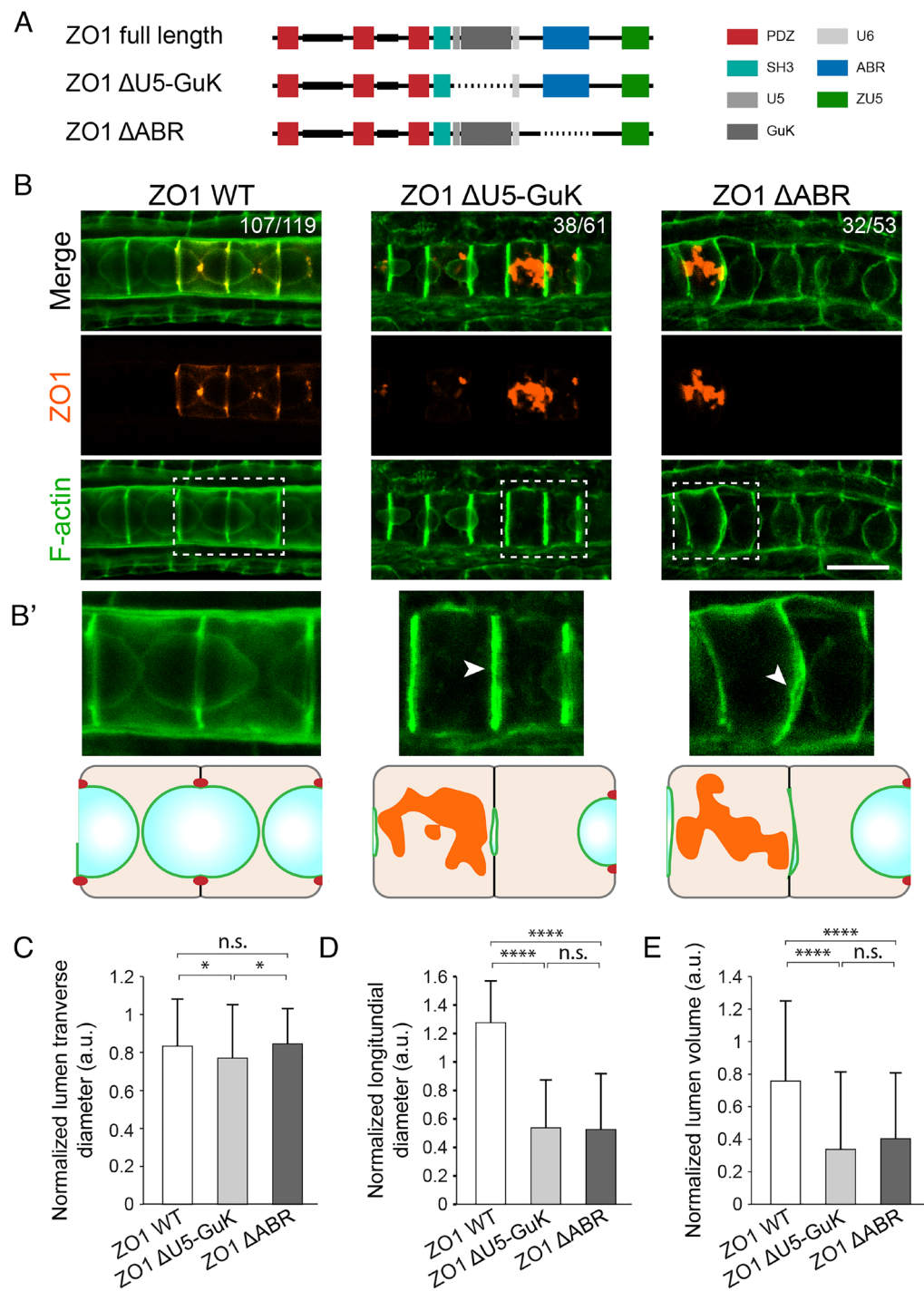


**Fig. 4.** Role of TJs as a physical barrier in notochord lumen expansion. (A) Schematic representation of the domain structure of the full-length ZO1 construct, the ZO1 $^{\Delta}$ U5-GuK construct lacking its U5 and GuK regions, and the ZO1 $^{\Delta}$ ABR construct lacking the actin binding region (ABR). (B) Confocal images of notochord cells expressing of ZO1 wild type and ZO1 mutants fused to tdTomato, with F-actin (Phalloidin staining) showing the lumen and cell boundary ( $n = 119, 61, 53$  cells,  $N = 5, 5, 4$  embryo batches for ZO1 WT, ZO1 $^{\Delta}$ U5-GuK, ZO1 $^{\Delta}$ ABR-transfected groups, respectively). (B') Higher-magnification images of the boxed area highlight the lumen expansion failure phenotype. White arrowheads indicate the failure of lumen membrane opening. The cartoon shows an intuitive lumen structure in the ZO1 mutant positive cells. Red dots and shaded areas show the localization of ZO1 WT and mutants. (C) Quantification of normalized lumen TD of ZO1 wild-type and ZO1 mutants (mean  $\pm$  SD), showing slight or no significant difference ( $n = 14, 17, 17$  independent embryos,  $N = 5, 5, 4$  embryo batches for ZO1 WT, ZO1 $^{\Delta}$ U5-GuK, ZO1 $^{\Delta}$ ABR-transfected groups, respectively). (D) Quantification of normalized lumen LD of ZO1 wild-type and ZO1 mutants for the samples described in (C). (E) Quantification of normalized lumen volume of ZO1 wild-type and ZO1 mutants for the samples described in (C) (mean  $\pm$  SD), showing a significant reduction in ZO1 mutant cells. The Mann-Whitney *U*-test and Student *t* test are used, depending on whether data shows normality distribution (C-E). \**P* < 0.05, \*\*\*\**P* < 0.0001. [Scale bar, 20  $\mu$ m in (B).]

**Physical Model for Lumen Expansion.** To model the physics of lumen expansion in the *Ciona* notochord, we consider a theoretical framework that includes active mechanics and active transport. Mechanical stresses are relevant both at the cell–lumen interface and at the contact point where two neighboring cells meet the lumen. We explore several potential mechanisms through which the cell may regulate the forces, including the dynamics of the actomyosin ring and the stability of TJs. In addition to these mechanical considerations, we also examine ion and water transport regulated by the cells in contact with the lumen. These hydraulic properties are also regulated, and we further consider the role of active ion pumps and vesicle trafficking, which may directly contribute to active water flux into the lumen.

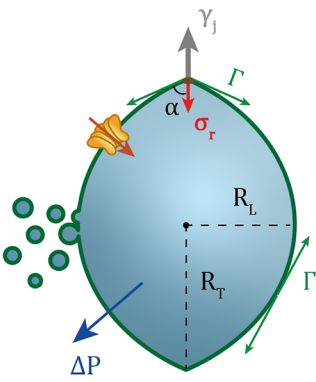
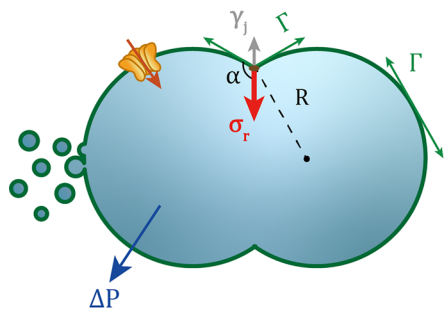
For simplicity, we discuss the case of a lumen composed of two identical spherical caps with a radius of  $R(t)$  and a contact angle of  $\alpha(t)$  (Fig. 5A). The case of an asymmetric lumen is described in *SI Appendix, Details of the Theoretical Model for the Lumen Dynamics*.

We first discuss the mechanical properties of the system. Given that inertia can be neglected, normal stress balance is satisfied at all times at the cell/lumen interface. Therefore, the hydrostatic pressure difference  $P^{lumen} - P^{cell} = \Delta P$  obeys Laplace law:

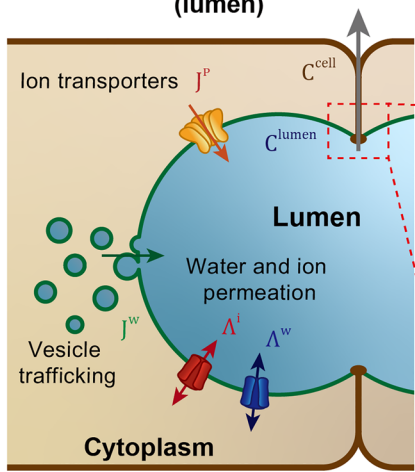
$$P^{lumen} - P^{cell} = \frac{2\Gamma}{R(t)}, \quad [1]$$

where  $R(t)$  is the radius of the spherical caps forming the lumen, and  $\Gamma$  is an effective surface tension that accounts for the

### A Force analysis (2D) and geometrical coefficients



### B Transport coefficients (lumen)



### C Transport coefficients (cleft)

**Fig. 5.** Schematic of the tube expansion model between two notochord cells. (A) Force analysis and definition of lumen geometrical parameters under spherical cap simplification. The green curved line, green circles, and blue area indicate the apical domain, vesicle trafficking, and luminal fluid (extracellular space), respectively. (B) Definitions of active transport coefficients and passive permeation coefficients at the apical domain. (C) Definitions of passive leak and TJs gate barrier function at the cell–cell cleft. We defined: the radius of curvature  $R$ ; the lumen contact angle  $\alpha$ ; the lumen boundary ring tension  $\sigma_r$ ; the surface tension at the cell–lumen interface  $\gamma_j$ ; the active water flux due to vesicle trafficking  $J^w$ ; the active pumping rate  $J^p$ ; the hydrostatic pressure difference between the extracellular lumen and cytoplasm  $\Delta P$ ; the ion and water permeation coefficients, respectively  $\Lambda^i$  and  $\Lambda^w$ ; and the ion and water leak fluxes through the cell–cell cleft, respectively,  $j_p$  and  $j_p^w$ .

contractility of the cell actomyosin cortex. Forces are also balanced at the junction where the two cells and lumen meet, according to the Young–Dupré relation:

$$\Gamma \cos \alpha(t) + \frac{\sigma_r}{R_T(t)} = \gamma_j, \quad [2]$$

where  $R_T(t) = R(t) \sin \alpha(t)$  represents the radius of the contractile ring surrounding the lumen at the intersection of the two spherical caps (the transverse radius of the lumen), and  $\sigma_r$  is its line tension. We denote by  $\gamma_j$  the tension due to TJs. Based on the experimental evidence discussed above, we anticipate that both  $\sigma_r$  and  $\gamma_j$  are under cellular control and play a pivotal role in regulating notochord lumen expansion.

Active pumping is described within an irreversible thermodynamics framework. Cells actively pump ions, which in turn creates an osmotic pressure difference leading to (passive) water flux (Fig. 5B). Water flux is thus driven by two thermodynamic forces: hydrostatic and osmotic pressure differences. Thus, the dynamics of the lumen volume  $V(t) = 2\pi R(t)^3 (2 + \cos \alpha(t)) (1 - \cos \alpha(t))^2 / 3$  obey:

$$\frac{dV}{dt} = A j_A^w - \mathcal{P} j_P^w, \quad [3]$$

where  $A = 4\pi R(t)^2 (1 - \cos \alpha(t))$  and  $\mathcal{P} = 2\pi R(t) \sin \alpha(t)$  denote the lumen surface area and perimeter, respectively. The effective water flux  $j_A^w = \Lambda^w (\Delta \Pi - \Delta P) + J^w$  accounts for passive flux through aquaporins in the first term with  $\Lambda^w$  the membrane

permeability to water flows, while the second term describes a constant active flux due, for instance, to vesicle trafficking. The passive flux is driven by hydrostatic and osmotic pressure differences, with the osmotic pressure difference  $\Delta \Pi = \Pi^{lumen} - \Pi^{cell} = k_B T \Delta C$ , where  $k_B$  is the Boltzmann constant,  $T$  the temperature and  $\Delta C = C^{lumen} - C^{cell}$  denotes the concentration difference between the lumen and the cell. Furthermore, the lumen transverse radius cannot exceed the size  $L$  of the cell, and we expect leaks to become important when  $R_T \sim L$ . Therefore, we introduced  $j_P^w = \frac{j_P^{w,0}}{L - R_T}$  to account for water leak from the cleft (Fig. 5C).

Finally, an osmotic pressure difference arises due to active cell pumping. For simplicity, we consider the transport of a single ionic species here. The number  $N(t)$  of ions in the lumen evolves according to

$$\frac{dN}{dt} = A j_A - \mathcal{P} j_P, \quad [4]$$

where the ion flux  $j_A = \Lambda^i (\mu^{cell} - \mu^{lumen}) + J^p$  is due to ion transport through channels and pumps on the membrane. We have defined  $\Lambda^i$  as the membrane permeability to ion flows, and  $\mu^{cell} - \mu^{lumen} \approx -k_B T \Delta C / C^{cell}$  represents the chemical potential difference between the cell and lumen. The flux due to active pumps is captured by  $J^p$  (positive when the flux is from the cell to the lumen). Similar to the volume leak term, we also have an ion leak term with  $j_P = \frac{j_P^0}{L - R_T}$ . We provide a detailed analysis of the model,

its steady-state and their stability (*SI Appendix*, Fig. S9) in *SI Appendix*. In *SI Appendix*, Tables S1 and S2, we provide a summary of the different parameters used in the model and an estimation of their values. We detail in the next section how the fitted values are obtained. We checked that the model parameter values used in all the scenarios and perturbations that we discuss in the following remained within the biological range reported in the literature.

**Recapitulating *Ciona* Notochord Lumen Expansion from the Model.** In order to compare our model with experiments and to make further predictions, we then fitted the experimental data obtained during *Ciona* notochord lumen expansion to calibrate the model parameters. The following strategy was used. First, we fitted the value of the tensions at the junction. At each time point during lumen expansion, the actomyosin ring contractility tension  $\sigma_r(t) = \Sigma_r I(t)$  is obtained from the relative fluorescence intensity at the lumen boundary  $I(t)$  (Fig. 2*J*) multiplied by a global magnitude coefficient  $\Sigma_r$ , which is the first fitting coefficient. Using the experimental values for the lumen radius  $R(t)$ , we applied the Young–Dupré equation [2] to obtain the best fit values for the lumen surface tension  $\Gamma$  and the TJ tension  $\gamma_j$  that align with the experimentally measured contact angle  $\alpha(t)$ . We assumed the lumen surface tension  $\Gamma$  to be constant during the expansion, while a fixed value of TJ tension  $\gamma_j$  was insufficient to explain the change in contact angle from the experiments. Thus,

we considered that the TJ tension  $\gamma_j$  may vary as a function of time. To limit the number of fitting parameters, and considering that *Ciona* notochord lumen expansion can be divided into three main phases, we used one parameter  $\gamma_j^{(i)}$  for each of these phases ( $i = 1, 2, 3$ ), and applied a smooth polynomial interpolation between each phase (*SI Appendix*). The best fit results for  $\gamma_j^{(i)}$ ,  $\Gamma$ , and  $\Sigma_r$ , and the corresponding lumen shapes during growth are shown in Fig. 6 *A* and *B*.

Next, we fitted the parameters associated with lumen hydraulics. Because of the arrested dynamics of the lumen at phase II, the hydraulic equations [3 and 4] with fixed values for the parameters cannot explain the observed growth of the *Ciona* notochord lumen. Given that active ion pumping is the primary factor for establishing osmotic pressure, we postulated that cells may vary their active pumping rate  $J^p$  over time. Similarly to the procedure for the TJ tension, we therefore introduced three values  $J^p, (i)$  of the active pumping rate for each phase  $i = 1, 2, 3$  (*SI Appendix* for details). The best fit for  $J^p$  is shown in Fig. 6*C* and Movie S2. The values of the fitting parameters obtained after the two subsequent fitting steps are summarized in *SI Appendix*, Table S2.

We can then compare the lumen dynamics from the theoretical model with the experimental data. A good agreement between the model and the experimental data during all three phases is displayed in Fig. 6 *D–F*. The model then allows us to draw conclusions on the typical characteristics of *Ciona* notochord lumen growth. In phase I

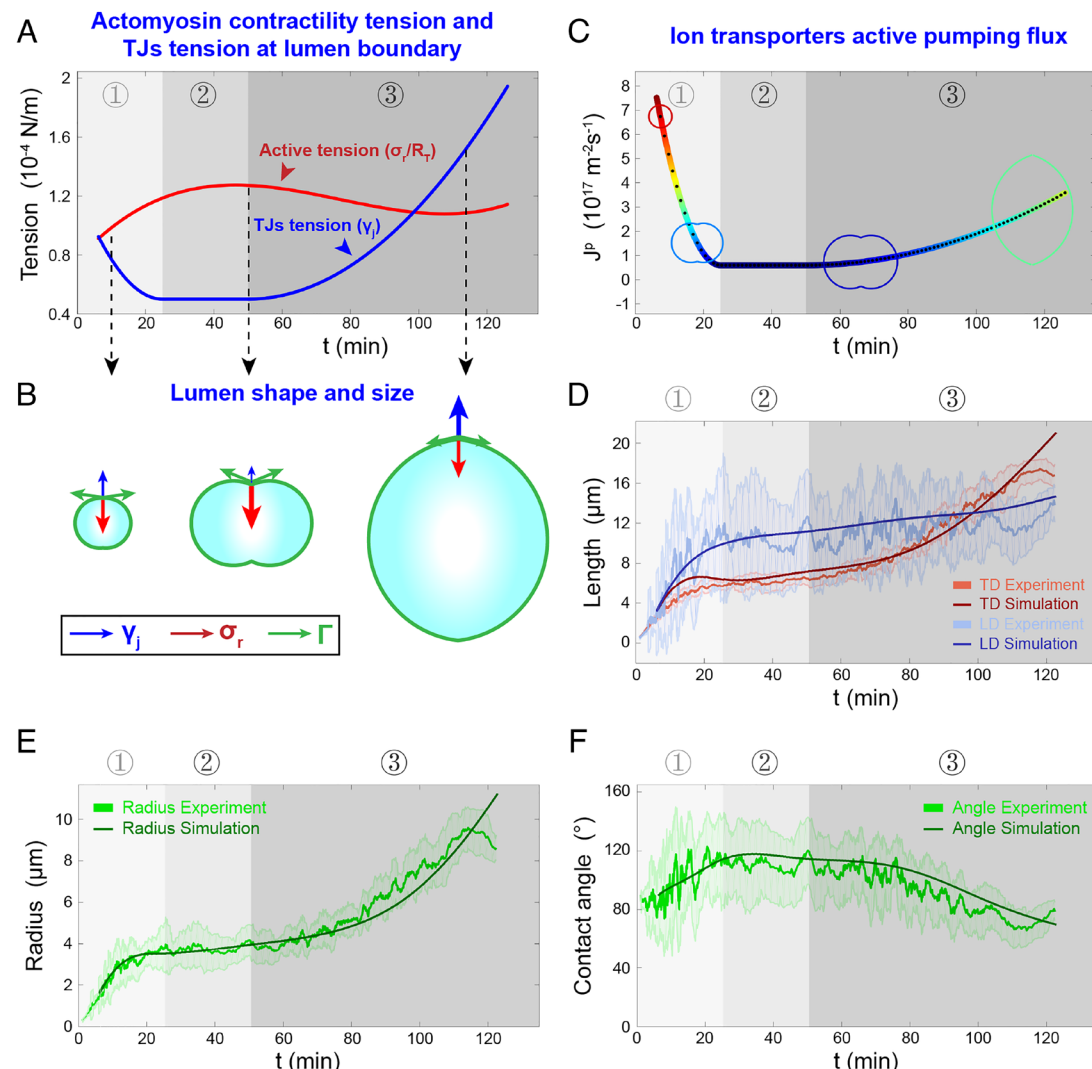


**Fig. 6.** Estimation of the relative parameters through the minimalistic tube expansion model. (A and B) Force balance between the lateral actomyosin ring active contractility tension (red) and TJ tension (blue) at the cell-cell junction for different lumen shapes and sizes, corresponding to the three phases of the lumen expansion. Active ring contractility tension is deduced from the actomyosin relative fluorescence intensity at the lumen boundary, while TJ tension is considered as a time-dependent tension with three phases, and is fitted based on the lumen growth dynamics. (C) Polynomial fit of the active ion pumping rate as a function of time (see *SI Appendix* for details). Spherical caps at different time points show lumen geometry and relative size. (D) Transverse lumen diameter (TD, red) and longitudinal lumen diameter (LD, blue) as a function of time in the experiments and from the model (darker solid lines). (E) Lumen radius as a function of time in the experiments and from the model. (F) Contact angle as a function of time in the experiments and from the model.

(corresponding to 0 to around 25 min), which is the lumen nucleation and initial period of lumen expansion, a high TJ tension coupled with highly active ion transport aids the lumen to open quickly, giving an overall prolate shape to the lumen made of two spherical caps. In phase II (corresponding to 25 to around 60 min), a low value of the ion pumping rate stabilizes the lumen, while high ring tension and low TJ tension result in a peanut-like lumen geometry with a large contact angle ( $\alpha < 90^\circ$ ). In phase III (corresponding to 60 to around 126 min), which is the maturation period of tube expansion, an increasing active pumping facilitates rapid lumen expansion, while high TJ tension stretches the lumen, which may be beneficial for the tube tilting and connecting process (12).

**Understanding Perturbed Lumen Expansion Dynamics from the Model.** Having considered the WT tube expansion kinetics, we then considered whether our model could help understand biological perturbations. We focus on perturbations that were performed in a previous publication (31), for which a dynamical quantification of the lumen expansion was available, and we also discuss the experimental data presented above in the light of the model.

**Perturbation of the acto-myosin cortex contractility with blebbistatin.** We first focus on the case studied in a previous paper, where cells were treated with blebbistatin (31), a drug that decreases acto-myosin contractility by inhibiting myosin activity (48). In this experiment, lumen formation dynamics was largely modified:

throughout the expansion, the lumen remained lens-shaped, with a larger TD compared to WT, while the LD was smaller (Fig. 7A, purple dots) and an overall smaller lumen volume. Interestingly, the growth was more steady and the three phases of the WT expansion can hardly be identified. To recapitulate this lumen expansion dynamics from the model, we decreased both the lateral ring contractility and the tension at the lumen surface. Consistently with the absence of growth phases, the best fits of our model were obtained when considering a constant value for all the parameters of the model (Fig. 7A, purple solid line and *SI Appendix* for details). **Overexpression of active ion transporters.** We then considered the overexpression of the anion transporter Slc26aa, that was required for lumen expansion (49). Intuitively, we expected that such a perturbation would allow for larger osmotic pressure differences, and therefore larger lumen volumes. This was indeed observed in the experiments (31), where the perturbed lumen size was always larger than the WT lumen at all time during the dynamics (Fig. 7B and ref. 31). We went further by comparing the perturbed dynamics of the lumen expansion with our model. In order to match the angle dynamics and satisfy Young–Dupré relation, we noted that the tension at the cell–cell junction had to be modified compared to WT (*SI Appendix*, Fig. S10). The active pumping rate was also modified compared to WT to match the experimental dynamics. Since the perturbed lumen at the first available time point was already larger than the WT, it suggests that the initial

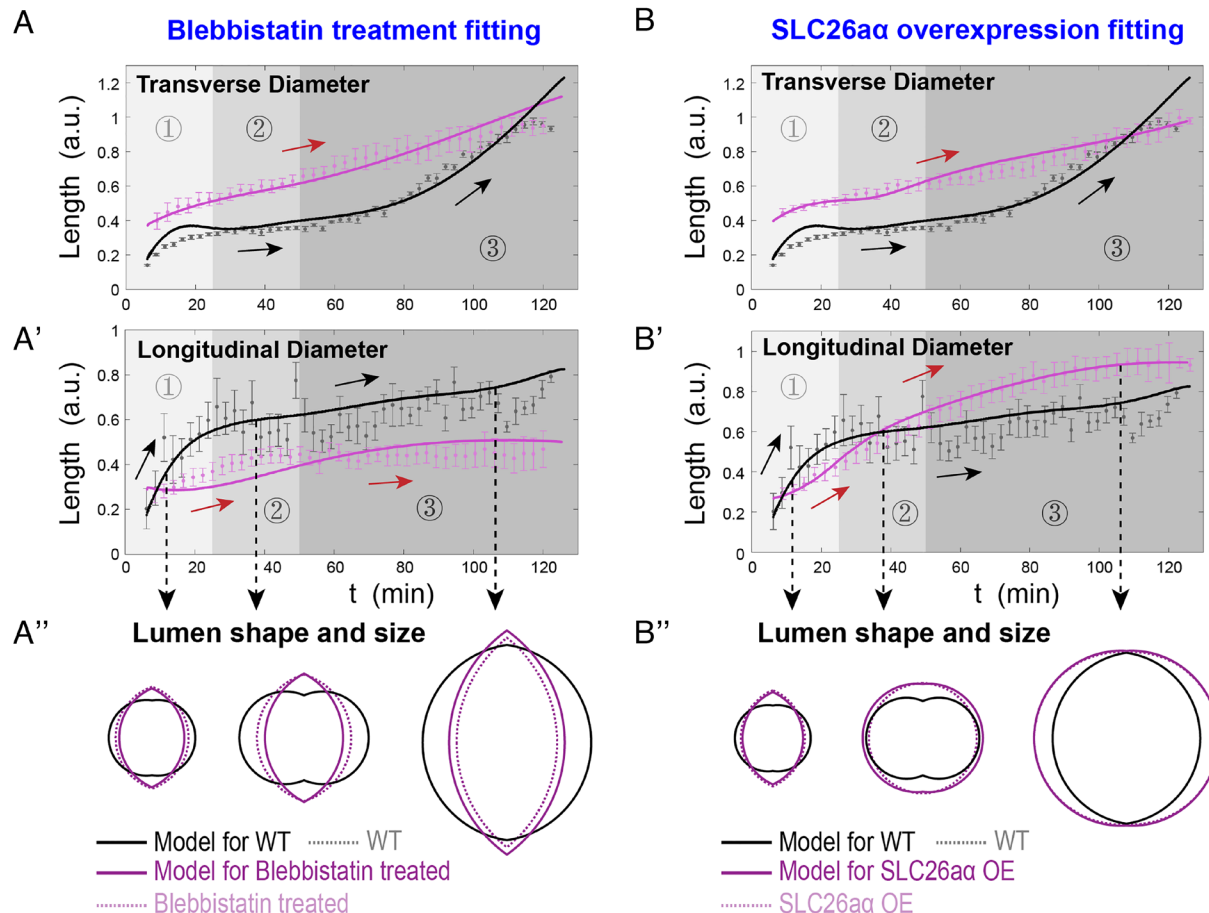


**Fig. 7.** Using model predictions to understand two biological perturbations. Experimental data (dots representing mean  $\pm$  SD, data from ref. 31) and model predictions (solid lines) for the dynamics of the TD and LD are shown as a function of time. The perturbations are displayed in purple and can be compared with WT in black. (A–A'') Perturbation of lumen growth by blebbistatin treatment. In the perturbed model, all the active contractile tensions and ion pumping rate are decreased compared to WT. In addition, all parameters are considered constant in time and do not depend on the three phases discussed in the WT. (B–B'') Perturbation of lumen growth after SLC26aa overexpression. In the perturbed model, TJ tension is fitted to match the angle dynamics and satisfy Young–Dupré relation, and ion pumping rate is two times larger than WT at first and steadily decreases (see *SI Appendix*, Fig. S11 for their precise value as a function of time). In addition, lumen surface tension is 1.5 times larger than WT.

active pumping rate is larger than steady-state value in WT, and then steadily decreases (*SI Appendix*, Fig. S10).

#### Perturbation of asymmetric tension by overexpression of Cdc42-DN.

We also considered the Cdc42 perturbation discussed in this paper. In most cases, this phenotype was too severe to make quantitative predictions. However, as discussed above, we noticed that in rare cases where a lumen did form (Fig. 3 A, Bottom Right), it was abnormally elongated in the longitudinal direction of the Cdc42-DN transfected cells. This can be rationalized by the fact that the acto-myosin cortex contractility was likely decreased in this transfected cell compared to the contractility of the neighboring cell that was not expressing Cdc42. In *SI Appendix*, we discussed this asymmetrical scenario, where the two cells enclosing the lumen have different properties, and in particular, different tensions. From our model, we indeed expect an asymmetric lumen, more elongated in the less contractile cell (*SI Appendix*, Fig. S12).

**ZO1 perturbation and leaks at cell-cell junctions.** Finally, we revisited the data presented in Fig. 4 where the TJ protein ZO1 was compromised. Since TJs likely play a fundamental role in limiting leaks at cell–cell junction, we thus considered the situation in the model where the paracellular leak term increases (Fig. 8A). It led to a stronger passive leak of ions and water, and the model thus predicts a lumen with significantly smaller volume, which is consistent with the data presented in Fig. 4. In addition, if the leak term is increased further, the model predicts a collapse of the lumen (*SI Appendix*, Fig. S13H), which is similar to the phenotype observed in the experimental data shown in Fig. 4B where lumens fail to open and grow. Note that decreasing the leak term in the model, which could mean more or tighter TJs, leads to a larger lumen volume. This is not what we observe experimentally, where overexpression of ZO1 does not lead to a significant change in lumen volume. This suggests that the cell–cell cleft cannot be made tighter by adding more TJs.

**Using the Model for Predictions.** Since our model has proven effective in recapitulating WT and perturbed lumen dynamics, we then used it to predict the tube expansion in cases where experimental data is not yet available.

**Hydraulic perturbations.** We first considered two hydraulic perturbations: i) vesicle trafficking (active water flux) increase or decrease (Fig. 8B) and ii) decrease of the membrane permeability (Fig. 8C). In case (i), the model predicts that the lumen volume growth rate increases, leading to a larger TD and LD compared to WT. The lumen is thus larger at all stages while its shape remains similar to WT. Decreasing the active water flux compared to WT has a limited effect with only a slight decrease of the volume. In case (ii), decreasing the membrane permeability slows down the passive ion flow across the apical membrane, and leads to an increase in osmotic pressure difference. The model thus predicts a trend opposite to situation (i), where active fluxes due to vesicle trafficking are decreased.

**Mechanical perturbations.** We have discussed above experiments where acto-myosin activity was globally reduced. Here, we use our model to perturb contractility at specific locations. We considered i) a modified contractile ring tension (*SI Appendix*, Fig. S12A) and ii) a perturbed spatial distribution of the acto-myosin cortex (*SI Appendix*, Fig. S12 B–D). In scenario (i), an increased ring tension leads to an exaggerated pinching of the lumen and to more transversally elongated final shapes. This is in line with the phenotype observed in our previous study on the overexpression of MRLC T18E-S19E (31), and it strengthens the hypothesis that its overexpression leads to an increased ring tension (31). Conversely, when ring tension is lowered, a limited LD expansion is observed. In scenario (ii), we explored perturbations of the equatorial contractile ring, which has been shown to drive precisely the elongation of notochord cells (50). Considering a fixed total cortex mass in the model, we increased cortex density at the equator (*SI Appendix*, Fig. S12B), which leads to a decreased density in other areas (*SI Appendix*, Fig. S12 B, Right). Such perturbation lowers the lateral ring tension, hence reducing the pinching of the lumen and leading to smaller LD, while the TD remains relatively comparable to WT. Conversely, an increase of cortex density at the lateral ring (*SI Appendix*, Fig. S12C) causes the lumen to be overconstrained and larger LD is obtained. We also considered an increase of the cortex density diffusion coefficient during phase III (*SI Appendix*,

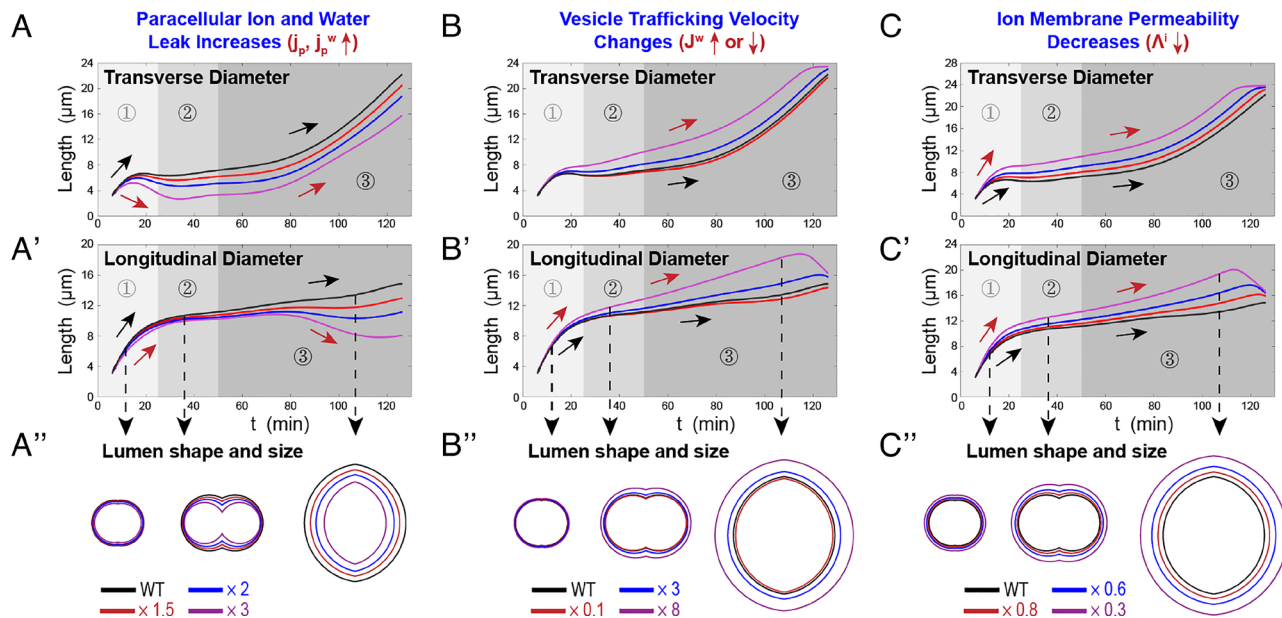


**Fig. 8.** Alternative models elucidate the function of each model parameter or biological regulation process on tube expansion. Lumen growth dynamics, including TD and LD, are predicted under different conditions. WT condition is shown in black, and perturbations of different magnitude (indicated in the last subpanel) compared to WT are in different colors. (A–A') Model predictions when both ion and water leak through the paracellular cleft increases, while all other conditions remain the same as the WT. (B–B'') Active water flux due to vesicle trafficking is decreased (red line) or increased (blue and magenta lines). (C–C'') Ion membrane permeability coefficient is decreased, leading to a slower passive ion flux through the apical membrane.

**Fig. S12D**), which leads to a delay in the elongation of the TD compared to WT and to a more pronounced pinching of the lumen. **Stability range of the lumen.** Finally, our model can assist us in determining the theoretical range of model parameters that ensure proper lumen formation and expansion (*SI Appendix*, Fig. S13). First, the lateral contractile ring tension needs a precise regulation. We observe that an excessive contractility—with a threshold that we estimate to be of the order of ~170% of the WT—would eventually split the lumen into two disconnected parts (*SI Appendix*, Fig. S13A and Movie S3). Second, active ion and water fluxes also need to be controlled within a reasonable range: if the ion transporters pumping rate were ~60% lower compared to WT, or if the ion membrane permeability coefficient were ~400% higher, the lumen could become too small, and eventually split into two disconnected parts due to the tension at the lumen boundary (*SI Appendix*, Fig. S13 B and G and Movie S4). Similarly, if the active water flux due to vesicle trafficking decreases or increases, the lumen also becomes smaller or larger (*Movie S5*). Finally, we note that an excessive paracellular leaks—larger than ~3 times that of the WT—would lead to the collapse of the lumen and would prevent proper tube expansion (*SI Appendix*, Fig. S13H and Movie S6).

## Discussion

In this study, we established that the tubular lumen structure opening and expansion in the *Ciona* notochord is under precise and dynamic cellular control. Our data revealed that the sequential dynamics of tube expansion, with three main phases, stem from the precise regulation of active contractility tension at the tube boundary, leading for instance to a characteristic peanut shape of the lumen at phase II, and a precise regulation of active transport and pumping activity, guaranteeing lumen growth and expansion during phases I and III.

We screened upstream Rho signaling and determined that Cdc42 is a key regulator of the tube formation and expansion: its misregulation can significantly alter the cortex distribution in the basal-lateral domain, and even compromise the very formation of the tube. We further demonstrated the critical role of TJs for notochord tube expansion, as they guarantee the tightness of the lumen and limit paracellular leaks. We showed that TJ disruption can prevent lumens from opening.

Based on the experimental data available for the *Ciona* notochord lumen, we constructed a physical model based on active mechanics and their interplay with active ion and water transport at the cell–lumen. The model parameters were estimated from the existing literature or fitted based on the three-phase dynamics of the wild type lumen growth. Furthermore, we used our model to recapitulate the tube expansion dynamics in two perturbed cases, for which tube expansion dynamics data was available (31): i) blebbistatin-treated cells, which showed an important decrease of their contractile activity as well as a lack of sequential dynamics compared to wild type; ii) overexpression of the anion transporter Slc26a $\alpha$ , where pumping activity is increased and leads to oversized lumens. Our model also allowed us to explore the role of each parameters separately, suggesting that disruptions in the regulation of lumen boundary tension or changes in ion and volume control can induce tube expansion instability or even failure, consistent with previous experimental results (31, 49, 51). We further calculated the theoretical boundaries of the model parameters that allow for successful lumen expansion. Our results suggest that the sequential tube expansion has nothing stochastic but is rather precisely regulated, indicating that such tube expansion dynamics contribute to stability in organogenesis.

Our findings highlight that the tension of the lateral actomyosin ring is closely linked to tube growth and geometry. While the tube structure in the *Ciona* notochord is unique, actin rings have been shown to play a similar role in various tubular systems. For instance, the formation of actin rings regulates tracheal morphogenesis in *Drosophila* (52). Actin rings also function as a zipping mechanism to drive embryo sealing during blastocyst formation (53). In our research, we observed a strong correlation between actomyosin ring overactivity and tube contact angle, consistent with the laws of mechanics at contact points, and unveiling a potential underlying mechanism by which the actomyosin ring regulates tube geometry. This is consistent with the fact that Rho signaling has been proven critical for lumen expansion: in an in vitro system, inhibition of the ROCK–myosin-II pathway leads to a multiple lumens phenotype in MDCK cells (54). In our current study, we identified that the actin cytoskeleton is downstream of Cdc42 in the *Ciona* notochord, which is one of the decisive factors controlling tube expansion.

Our theoretical model integrates cell mechanics and hydraulics, aligning with earlier works on lumen growth in cells (22) and tissues (55–57). However, we enhance these approaches by emphasizing the crucial role of actomyosin ring tension. This tension enables a “pinched prolate” (peanut-like) shape of the lumen with a high contact angle, a shape that would otherwise be unattainable. Furthermore, our model and experimental data underscore the significance of the temporal regulation of this ring tension. This regulation ultimately leads to three distinct phases in the lumen growth that are under stringent cellular control.

Our current model takes into account the multifunction role of vesicles in tube expansion. One of the most significant functions is to deliver apical membrane materials to facilitate the expansion of new luminal space (2). During mouse blastocyst formation, cytoplasmic vesicles are actively secreted into the lumen space, and Brefeldin A treatment significantly reduces lumen volume (10). Our recent work in *Ciona* notochord and *Drosophila* trachea also demonstrated that the secretory pathway is necessary for lumen inflation (58–60).

Furthermore, our model underscores the importance of TJs in tube opening and expansion. TJs serve to prevent biomacromolecules from diffusing outside the lumen space and act as a barrier for the diffusion of various classes of ions (61, 62), therefore aiding in stabilizing lumen dynamics. The TJs ring also functions as a physical boundary of the apical domain in the notochord system. The mechanosensitive property of TJs (63) may help to explain the lag stage of the TD as the contractile ring tension reaches its peak in phase II. Moreover, TJs serve as an intracellular signaling center, regulating the localization and activity of small Rho GTPases, such as RhoA and Cdc42 (64). Based on the interaction between TJs and Rho GTPases and the mechanosensation of TJs, the lumen formation process and notochord cell elongation can form a mechanosensitive feedback loop that may aid in regulating notochord morphogenesis.

## Materials and Methods

The animal culture, embryo manipulation, and plasmid construction followed the previous procedures (65). Quantification and statistical analysis processing of experimental data were performed using Fiji (NIH, <https://fiji.sc/>) (66) and/or processed using custom-made MATLAB code. Additional details of materials and methods can be found in *SI Appendix, Materials and Methods*. The definition and estimated value of dimensionless parameters for theoretical model and the plasmid primer information are provided in *SI Appendix, Tables S3 and S4*, respectively.

**Data, Materials, and Software Availability.** The plasmids and any information required to reanalyze the data reported in this paper will be shared by the lead contact. The original code for MATLAB and Mathematica used in this paper are available on a Github repository (67). The raw confocal images of tube formation of wild type and perturbations used in this study are available on a Zenodo repository (68).

**ACKNOWLEDGMENTS.** This work was funded by the Science & Technology Innovation Project of Laoshan Laboratory (Nos. LSKJ202203204 and LSKJ202203002), the National Key Research and Development Program of China (2022YFC2601302), and the Taishan Scholar Program of Shandong Province,

China (B.D.). We acknowledged the support of the High-Performance Biological Supercomputing Center at the Ocean University of China for this research.

Author affiliations: <sup>a</sup>Fang Zongxi Center for Marine EvoDevo, Ministry of Education Key Laboratory of Marine Genetics and Breeding, College of Marine Life Sciences, Ocean University of China, Qingdao 266003, China; <sup>b</sup>Laboratory for Marine Biology and Biotechnology, Qingdao Marine Science and Technology Center, Qingdao 266237, China; <sup>c</sup>Laboratoire Physique des Cellules et Cancer (PCC), CNRS UMR 168, Institut Curie, Université Paris Sciences et Lettres, Sorbonne Université, Paris 75005, France; <sup>d</sup>Mechanobiology Institute, National University of Singapore, Singapore 117411, Singapore; and <sup>e</sup>Institute of Evolution and Marine Biodiversity, Ocean University of China, Qingdao 266003, China

1. B. Lubarsky, M. A. Krasnow, Tube morphogenesis: Making and shaping biological tubes. *Cell* **112**, 19–28 (2003).
2. S. Sigurbjörnsdóttir, R. Mathew, M. Leptin, Molecular mechanisms of de novo lumen formation. *Nat. Rev. Mol. Cell Biol.* **15**, 665–676 (2014).
3. A. W. Overeem, D. M. Bryant, S. C. D. van IJzendoorn, Mechanisms of apical–basal axis orientation and epithelial lumen positioning. *Trends Cell Biol.* **25**, 476–485 (2015).
4. A. J. Blasky, A. Mangan, R. Prekeris, Polarized protein transport and lumen formation during epithelial tissue morphogenesis. *Annu. Rev. Cell Dev. Biol.* **31**, 575–591 (2015).
5. C. Zihni, C. Mills, K. Matter, M. S. Balda, Tight junctions: From simple barriers to multifunctional molecular gates. *Nat. Rev. Mol. Cell Biol.* **17**, 564–580 (2016).
6. T. Otani, M. Furuse, Tight junction structure and function revisited. *Trends Cell Biol.* **30**, 805–817 (2020).
7. Q. Li *et al.*, Extracellular matrix scaffolding guides lumen elongation by inducing anisotropic intercellular mechanical tension. *Nat. Cell Biol.* **18**, 311–318 (2016).
8. C. Camelo, S. Luschnig, Cells into tubes: Molecular and physical principles underlying lumen formation in tubular organs. *Curr. Top. Dev. Biol.* **143**, 37–74 (2020).
9. C. J. Chan, T. Hiragi, Integration of luminal pressure and signalling in tissue self-organization. *Development* **147**, dev181297 (2020).
10. A. Q. Ryan, C. J. Chan, F. Gruber, T. Hiragi, Lumen expansion facilitates rpiBlast-primitive endoderm fate specification during mouse blastocyst formation. *Dev. Cell* **51**, 684–697.e684 (2019).
11. E. Hannezo, C. P. Heisenberg, Mechanochemical feedback loops in development and disease. *Cell* **178**, 12–25 (2019).
12. B. Dong *et al.*, Tube formation by complex cellular processes in *Ciona intestinalis* notochord. *Dev. Biol.* **330**, 237–249 (2009).
13. R. A. Frizzell, J. W. Hanrahan, Physiology of epithelial chloride and fluid secretion. *CSH Perspect. Med.* **2**, a009563 (2012).
14. K. R. Mosaliganti *et al.*, Size control of the inner ear via hydraulic feedback. *eLife* **8**, e39596 (2019).
15. I. A. Swinburne *et al.*, Lamellar projections in the endolymphatic sac act as a relief valve to regulate inner ear pressure. *eLife* **7**, e37131 (2018).
16. A. Dasgupta *et al.*, Cell volume changes contribute to epithelial morphogenesis in zebrafish Kupffer's vesicle. *eLife* **7**, e30963 (2018).
17. C. J. Chan *et al.*, Hydraulic control of mammalian embryo size and cell fate. *Nature* **571**, 112–116 (2019).
18. H. S. Ewart, A. Klip, Hormonal regulation of the Na<sup>+</sup>-K<sup>+</sup>-ATPase: Mechanisms underlying rapid and sustained changes in pump activity. *Am. J. Phys.* **269**, C295–C311 (1995).
19. E. Latorre *et al.*, Active superelasticity in three-dimensional epithelia of controlled shape. *Nature* **563**, 203–208 (2018).
20. N. L. Simmons, Ion transport in 'tight' epithelial monolayers of MDCK cells. *J. Membrane Biol.* **59**, 105–114 (1981).
21. M. Bagnat, I. D. Cheung, K. E. Mostov, D. Y. Stainier, Genetic control of single lumen formation in the zebrafish gut. *Nat. Cell Biol.* **9**, 954–960 (2007).
22. S. Dasgupta, K. Gupta, Y. Zhang, V. Viasnoff, J. Prost, Physics of lumen growth. *Proc. Natl. Acad. Sci. U.S.A.* **115**, E4751–E4757 (2018).
23. D. M. Bryant *et al.*, A molecular network for de novo generation of the apical surface and lumen. *Nat. Cell Biol.* **12**, 1035–1045 (2010).
24. S. M. Krug, J. D. Schulze, M. Fromm, Tight junction, selective permeability, and related diseases. *Semin. Cell Dev. Biol.* **36**, 166–176 (2014).
25. M. Potente, T. Makinen, Vascular heterogeneity and specialization in development and disease. *Nat. Rev. Mol. Cell Biol.* **18**, 477–494 (2017).
26. S. Hayashi, B. Dong, Shape and geometry control of the *Drosophila* tracheal tube. *Dev. Growth Differ.* **59**, 4–11 (2017).
27. E. Hoijman, D. Rubbini, J. Colombelli, B. Alsina, Mitotic cell rounding and epithelial thinning regulate lumen growth and shape. *Nat. Commun.* **6**, 7355 (2015).
28. V. Gebala, R. Collins, I. Geudens, L. K. Phng, H. Gerhardt, Blood flow drives lumen formation by inverse membrane blebbing during angiogenesis *in vivo*. *Nat. Cell Biol.* **18**, 443–450 (2016).
29. E. Denker, D. Jiang, *Ciona intestinalis* notochord as a new model to investigate the cellular and molecular mechanisms of tubulogenesis. *Semin. Cell Dev. Biol.* **23**, 308–319 (2012).
30. L. Zhao *et al.*, Biodiversity-based development and evolution: The emerging research systems in model and non-model organisms. *Sci. China Life Sci.* **64**, 1236–1280 (2021).
31. E. Denker *et al.*, Regulation by a TGFBeta-ROCK-actomyosin axis secures a non-linear lumen expansion that is essential for tubulogenesis. *Development* **142**, 1639–1650 (2015).
32. Q. Lu, P. Bhattachan, B. Dong, Ascidian notochord elongation. *Dev. Biol.* **448**, 147–153 (2019).
33. E. Denker, I. Bocina, D. Jiang, Tubulogenesis in a simple cell cord requires the formation of bi-apical cells through two discrete Par domains. *Development* **140**, 2985–2996 (2013).
34. M. C. Marchetti *et al.*, Hydrodynamics of soft active matter. *Rev. Mod. Phys.* **85**, 1143–1189 (2013).
35. M. Murrell, P. W. Oakes, M. Lenz, M. L. Gardel, Forcing cells into shape: The mechanics of actomyosin contractility. *Nat. Rev. Mol. Cell Biol.* **16**, 486–498 (2015).
36. H. Turlier, B. Audoly, J. Prost, J. F. Joanny, Furrow constriction in animal cell cytokinesis. *Biophys. J.* **106**, 114–123 (2014).
37. B. A. Bryan, P. A. D'Amore, What tangled webs they weave: Rho-GTPase control of angiogenesis. *Cell. Mol. Life Sci.* **64**, 2053–2065 (2007).
38. H. Yoshizaki *et al.*, Activity of Rho-family GTPases during cell division as visualized with FRET-based probes. *J. Cell Biol.* **162**, 223–232 (2003).
39. W. M. Bement, H. A. Benink, G. von Dassow, A microtubule-dependent zone of active RhoA during cleavage plane specification. *J. Cell Biol.* **170**, 91–101 (2005).
40. M. Coisy-Quivy *et al.*, Identification of Rho GTPases implicated in terminal differentiation of muscle cells in ascidians. *Biol. Cell* **98**, 577–588 (2006).
41. S. Etienne-Manneville, A. Hall, Rho GTPases in cell biology. *Nature* **420**, 629–635 (2002).
42. R. G. Hodge, A. J. Ridley, Regulating Rho GTPases and their regulators. *Nat. Rev. Mol. Cell Biol.* **17**, 496–510 (2016).
43. W. M. Bement, A. B. Goryachev, A. L. Miller, G. von Dassow, Patterning of the cell cortex by Rho GTPases. *Nat. Rev. Mol. Cell Biol.* **25**, 290–308 (2024).
44. G. Kesavan *et al.*, Cdc42-mediated tubulogenesis controls cell specification. *Cell* **139**, 791–801 (2009).
45. C. G. Vasquez, V. T. Vachharajani, C. Garzon-Coral, A. R. Dunn, Physical basis for the determination of lumen shape in a simple epithelium. *Nat. Commun.* **12**, 5608 (2021).
46. D. B. Simon *et al.*, Paracellin-1, a renal tight junction protein required for paracellular Mg<sup>2+</sup> resorption. *Science* **285**, 103–106 (1999).
47. K. Sherrard, F. Robin, P. Lemaire, E. Munro, Sequential activation of apical and basolateral contractility drives ascidian endoderm invagination. *Curr. Biol.* **20**, 1499–1510 (2010).
48. M. Kovacs, J. Toth, C. Hetenyi, A. Malnasi-Csizmadia, J. R. Sellers, Mechanism of blebbistatin inhibition of myosin II. *J. Biol. Chem.* **279**, 35557–35563 (2004).
49. W. Deng *et al.*, Anion translocation through an SLC26 transporter mediates lumen expansion during tubulogenesis. *Proc. Natl. Acad. Sci. U.S.A.* **110**, 14972–14977 (2013).
50. I. M. Sehring *et al.*, An equatorial contractile mechanism drives cell elongation but not cell division. *PLoS Biol.* **12**, e1001781 (2014).
51. P. Bhattachan *et al.*, Ascidian caveolin induces membrane curvature and protects tissue integrity and morphology during embryogenesis. *FASEB J.* **34**, 1345–1361 (2020).
52. E. Hannezo, B. Dong, P. Recho, J. F. Joanny, S. Hayashi, Cortical instability drives periodic supracellular actin pattern formation in epithelial tubes. *Proc. Natl. Acad. Sci. U.S.A.* **112**, 8620–8625 (2015).
53. J. Zenker *et al.*, Expanding actin rings zipper the mouse embryo for blastocyst formation. *Cell* **173**, 776–791.e717 (2018).
54. M. Kim, A. M. Shawen, A. J. Ewald, Z. Werb, K. E. Mostov, P114RhoGEF governs cell motility and lumen formation during tubulogenesis through a ROCK-myosin-II pathway. *J. Cell Sci.* **128**, 4317–4327 (2015).
55. A. Torres-Sánchez, M. Kerr Winter, G. Salbreux, Tissue hydraulics: Physics of lumen formation and interaction. *Cell Dev.* **168**, 203724 (2021).
56. C. Duclat, J. Prost, F. Julicher, Hydraulic and electric control of cell spheroids. *Proc. Natl. Acad. Sci. U.S.A.* **118**, e2021972118 (2021).
57. C. Duclat, N. Sarkar, J. Prost, F. Julicher, Fluid pumping and active flexoelectricity can promote lumen nucleation in cell assemblies. *Proc. Natl. Acad. Sci. U.S.A.* **116**, 19264–19273 (2019).
58. Z. Wang *et al.*, Proteomic identification of intracellular vesicle trafficking and protein glycosylation requirements for lumen inflation in *Ciona* notochord. *Proteomics* **23**, e2200460 (2023).
59. X. Ouyang, B. Wu, H. Yu, B. Dong, DYRK1-mediated phosphorylation of endocytic components is required for extracellular lumen expansion in ascidian notochord. *Biol. Res.* **56**, 10 (2023).
60. B. Dong, K. Kakihara, T. Otani, H. Wada, S. Hayashi, Rab9 and retromer regulate retrograde trafficking of luminal protein required for epithelial tube length control. *Nat. Commun.* **4**, 1358 (2013).
61. R. H. Adamson *et al.*, Oncotic pressures opposing filtration across non-fenestrated rat microvessels. *J. Physiol.* **557**, 889–907 (2004).
62. I. Cattaneo *et al.*, Shear stress reverses dome formation in confluent renal tubular cells. *Cell Physiol. Biochem.* **28**, 673–682 (2011).
63. C. Schwayer *et al.*, Mechanosensation of tight junctions depends on ZO-1 phase separation and flow. *Cell* **179**, 937–952.e918 (2019).
64. C. Zihni, S. J. Terry, Rho GTPase signaling at epithelial tight junctions: Bridging the gap between polarity and cancer. *Int. J. Biochem. Cell Biol.* **64**, 120–125 (2015).
65. L. Christiaen, E. Wagner, W. Shi, M. Levine, Isolation of sea squirt (*Ciona*) gametes, fertilization, dechorionation, and development. *Cold Spring Harb. Protoc.* **2009**, pdb.prot5344 (2009).
66. J. Schindelin *et al.*, Fiji: An open-source platform for biological-image analysis. *Nat. Methods* **9**, 676–682 (2012).
67. W. Shi *et al.*, Physics\_tube. GitHub: [https://github.com/WenjieShi8514/Physics\\_tube](https://github.com/WenjieShi8514/Physics_tube). Deposited 10 January 2025.
68. W. Shi *et al.*, Images for wild type and perturbations of lumen in *Ciona* notochord. Zenodo. <https://doi.org/10.5281/zenodo.15005334>. Deposited 18 March 2025.